Ocean Engineering 164 (2018) 272–283

Contents lists available at ScienceDirect

Ocean Engineering

journal homepage: www.elsevier.com/locate/oceaneng

Numerical investigation of vortex-induced motions of a paired-column semi-submersible in currents

Weiwen Zhao[a], Lu Zou[a], Decheng Wan[a,*], Zhiqiang Hu[b]

[a] State Key Laboratory of Ocean Engineering, School of Naval Architecture, Ocean and Civil Engineering, Shanghai Jiao Tong University, Collaborative Innovation Centre for Advanced Ship and Deep-Sea Exploration, Shanghai, China
[b] School of Engineering, Newcastle University, Newcastle Upon Tyne, UK

ARTICLE INFO

Keywords:
Vortex-induced motions
Paired-column semi-submersible
Detached-eddy simulation
Overset grid
naoe-FOAM-SJTU solver

ABSTRACT

Vortex-induced motions (VIM) is becoming a noteworthy issue for column-stabilized floating platforms, mainly due to its substantial fatigue damage to risers and mooring system. The VIM of deep-draft semi-submersible is more complex than single column floaters because of the wake interference between columns, as well as the considerable yaw motions. In the present work, a numerical approach for simulating VIM of deep-draft semi-submersible is proposed. Specifically, detached-eddy simulation is used for turbulence modeling and dynamic overset grid technique is used for moving objects. Simulations for stationary drag and VIM of a model-scale paired-column semi-submersible are conducted with the proposed approach. The numerical results are compared with experimental data. Transverse, in-line and yaw motions are allowed during VIM simulations and are further analyzed in frequency domain by Fast Fourier Transform (FFT). Different VIM characteristics are observed at different current velocities. The work done by each component of the structure is also discussed. Flow visualizations are presented for better understanding of the wake interferences during VIM. The accuracy and reliability of the current numerical approach is assessed.

1. Introduction

Modern offshore structures are often designed to have deep draft stabilized columns and low gravitational center in order to suppress the wave-induced motions, especially for heave motions. These column structures are subject to motions that are induced by the periodical fluctuation forces and vortex shedding when currents velocities exceed a few knots. The term vortex-induced motions (VIM) is coined to describe the phenomenon due to the motions are caused by vortices. VIM is a matter of high complexity, mainly due to the high Reynolds-number turbulent flows around the floating structure with complex geometry, six-degrees-of-freedom motions that are determined by various kinds of forces such as hydrodynamic forces, mooring forces, gravitational forces, and the interaction between the fluids and structures. VIM is similar to vortex-induced vibrations (VIV). The latter generally represents the high frequency vibrations of rigid or flexible cylinders with large aspect ratio, such as risers and cables. In contrast, VIM describes the much longer period motions of large volume offshore structures, such as Spars, monocolumn, semi-submersibles, TLPs and buoys. In the oil drilling production environment, the floating structures are moored with mooring lines. The floating structure and mooring lines can be treated as a spring-mass system. When the frequency of external excitation (vortex shedding or transverse hydrodynamic force) is at or near the structural natural frequency of the system in still water, the storage of vibrational energy increases rapidly which produces large amplitude oscillations whose amplitude can be up to one diameter of the column. Unlike stationary cylinder whose shedding frequency is proportional to velocity, the shedding frequency of spring-supported cylinder is locked in one natural frequency of the cylinder. This so-called “lock-in” phenomenon greatly accelerates the fatigue failure of mooring and risers system and reduces the service life span of offshore platforms (van Dijk et al., 2003).

There have been plenty of studies on VIM for various kinds of offshore platforms, most of which are performed by means of model tests in towing tanks or numerical simulations based on Computational Fluid Dynamics (CFD). Geometric similitude is important for model test and is achieved by scaling not only model geometry but also appurtenance from prototype accurately. Another important aspect is dynamic similitude which requires the properly scale of natural periods, mass ratio and reduced velocities (Finnigan and Roddier, 2007). It is well known that it is impossible to keep both Reynolds and Froude number scaling for hydrodynamic model testing of offshore structures. VIM model tests

* Corresponding author.
E-mail address: dcwan@sjtu.edu.cn (D. Wan).

https://doi.org/10.1016/j.oceaneng.2018.06.023
Received 22 February 2018; Received in revised form 6 May 2018; Accepted 9 June 2018

apply Froude number scaling for hydrodynamic similitude due to the speed limitation of towing facilities. The scaling effect brought by Reynolds number has been addressed by Roddier et al. (2009). They conducted a series of model tests for the hard tank part of a Truss Spar model in three different scale ratios (three different Reynolds regimes) and concluded that there are little differences between sub-critical and super-critical regimes, which means Froude number scaling in terms of geometric and dynamic similitude is applicable for VIM.

Recently, numerical simulation based on CFD has been improved with the advancing of computer science and numerical modeling techniques. There have been significant progress in the application of CFD to predict deep-draft semi-submersible VIM (Kim et al., 2011, 2015; Tan et al., 2013; Lee et al., 2014; Antony et al., 2015a; Chen and Chen, 2016; Kara et al., 2016; Vinayan et al., 2015). The comparison of CFD results against model test data in these literature shows the capability of CFD in modeling VIM with remarkable accuracy. Most of the simulations were carried out with commercial CFD software, such as the finite element solver AcuSolve (Kim et al., 2011, 2015; Antony et al., 2015a; Vinayan et al., 2015) and the finite volume solvers Star-CCM+ (Tan et al., 2013; Antony et al., 2015a) and Fluent (Antony et al., 2015a; Kim et al., 2015). Exceptions are Lee et al. (2014) and Chen and Chen (2016) who investigated the round-corner effect and scale effect of VIM of a deep-draft semi-submersible at model scale and full scale using an in-house Finite-Analytic Navier-Stokes (FANS) code which solves Reynolds-Average Navier-Stokes (RANS) equations in curvilinear body-fitted coordinate system with overset structured grid capability. Rosetti et al. (2016) presented numerical simulations of VIM of a semi-submersible with circular columns in 0 and 45° current heading by using ReFRESCO which is an in-house viscous-flow CFD code that solves multiphase unsteady incompressible flows using Navier-Stokes equations. Recently, the open source CFD software OpenFOAM raises as a popular CFD software in both academia and industry due to its flexible and extensible design and good source code quality. It's easy and convenient to implement customized functionality based on the framework. Zhao et al. (2014) simulated VIM of a Spar platform in uniform currents using an in-house solver naoe-FOAM-SJTU which is developed based on OpenFOAM. The effectiveness of helical strake on suppressing VIM was discussed. Kara et al. (2016) calculated VIM of a paired-column semi-submersible based on OpenFOAM. They implemented an in-house 6 degree-of-freedom (6DoF) solver with nonlinear coupling of accelerations and velocities to solve the motions. The 6DoF solver has an interface for generalized external forces such as spring forces. They also highlighted the key aspects of CFD methodology for VIM simulations and concluded that the detached-eddy simulation (DES) is a powerful turbulence model in estimating response amplitude and periods.

In the present paper, the CFD simulation of a paired-column semi-submersible with eight-columns and squared-pontoon hull configuration is performed using the in-house CFD code naoe-FOAM-SJTU. To resolve the turbulent wake structures and predict the wake interference between columns and pontoons, a DES turbulence model (SST-DDES) is employed. An unstructured overset grid approach is adopted to avoid mesh distortion and to support the arbitrary large movements of the hull. Compared with the structured FANS code, the current unstructured FVM approach can easily generate mesh for complex geometries such as blisters and strakes attached to columns. It will also reduce computational cost compared with the FEM code AcuSolve. The present numerical results compare well with experimental data and simulation results from the RPSEA 5404 project (Gordon and Mostofi, 2014), which shows the validity of the current numerical approach on such VIM problems.

2. Mathematical models and numerical methods

The finite volume CFD solver naoe-FOAM-SJTU (Shen and Wan, 2013; Shen et al., 2015) is used to perform all simulations. The naoe-FOAM-SJTU was initially developed based on the open source platform OpenFOAM version 2.0.1. It was derived from *interDyMFoam* (a standard solver from OpenFOAM) with an in-house 6DoF solver based on Euler angles and a wave generation and absorption module for various types of regular and irregular waves common in marine and ocean engineering. Furthermore, the dynamic overset capability was implemented into the solver in coupled with Suggar (Noack, 2005) to facilitate large amplitude hull motions. Recently, the solver was upgraded to OpenFOAM version 3.0. Moreover, the solver was coupled with Suggar++ (Noack et al., 2009), an improved version of Suggar, to compute domain connectivity information (DCI), and to connect fields solutions among multiple overset mesh blocks. The naoe-FOAM-SJTU has been validated against a majority of steady and unsteady problems (Cao and Wan, 2010; Zhou et al., 2013; Wang et al., 2017).

2.1. Governing equations and turbulence modeling

The flow is treated as single-phase and incompressible. The continuity and momentum equations for turbulent flow in vectorial form are written as

$$\nabla\cdot\mathbf{U} = 0 \tag{1}$$

$$\frac{\partial\mathbf{U}}{\partial t} + \nabla\cdot(\mathbf{U}-\mathbf{U}_g)\mathbf{U} = -\frac{1}{\rho}\nabla p + \nabla\cdot(\nu_{eff}\nabla\mathbf{U}) + (\nabla\mathbf{U})\cdot\nabla\nu_{eff} \tag{2}$$

where, $\mathbf{U}$ is the fluid velocity and $\mathbf{U}_g$ is the grid velocity, p is the pressure and ρ is the fluid density. The effective viscosity is defined as $\nu_{eff} = \nu + \nu_t$, where ν is the molecular viscosity and ν_t is the turbulent eddy viscosity.

The delayed DES (DDES) formulation of $k-\omega$ shear stress transport (SST) model is employed for turbulence modeling. The SST model is a blended $k-\omega/k-\varepsilon$ model which has been proven to be robust and accurate for turbulent flows around complex geometries in industry. DDES is a hybrid RANS/LES method which combines the best practice of RANS and LES in a single solution strategy. In this study, SST-DDES solves flow field using $k-\omega$ SST model in the near wall regions and converts to LES subgrid-scale model in other regions after flow separation. The transport equations for SST in moving frame are given as

$$\frac{\partial k}{\partial t} + \nabla\cdot(\mathbf{U}-\mathbf{U}_g)k = \widetilde{G} - \frac{k^{3/2}}{l} + \nabla\cdot[(\nu+\alpha_k\nu_t)\nabla k] \tag{3}$$

$$\frac{\partial\omega}{\partial t} + \nabla\cdot(\mathbf{U}-\mathbf{U}_g)\omega = \gamma S^2 - \beta\omega^2 + \nabla\cdot[(\nu+\alpha_\omega\nu_t)\nabla\omega] + (1-F_1)CD_{k\omega} \tag{4}$$

where k is the turbulent kinetic energy and ω is the specific dissipation rate. The turbulence length scale l in SST model is defined as $l = l_{RANS} = \frac{k^{3/2}}{\beta^* k\omega}$. $\widetilde{G} = \min(\nu_t S^2, c_1\beta^* k\omega)$ is a production limiter to prevent the built-up of turbulence in stagnation regions. F_1 is a blending function from SST model (Menter et al., 2003). α_k, α_ω, β, and γ are constants which are computed by a blend via $c = c_1F_1 + c_2(1-F_1)$. The corresponding constants are obtained from Zhao and Wan (2016), Gritskevich et al. (2011).

SST-DDES modifies the length scale to become l_{DDES} which can be written as

$$l_{DDES} = l_{RANS} - f_d\max(0, l_{RANS} - C_{DES}\Delta) \tag{5}$$

where C_{DES} is the calibrated DES constant. Δ is the cube root of the cell volume. f_d is an empiric blending function defined as

$$f_d = 1 - \tanh\left[(C_{d1}r_d)^{C_{d2}}\right] \tag{6}$$

$$r_d = \frac{\nu_t + \nu}{\kappa^2 d_w^2\sqrt{0.5(S^2+\Omega^2)}} \tag{7}$$

Here $C_{d1} = 20$ and $C_{d2} = 3$ are two constants. S and Ω are strain rate and vorticity tensor invariants, $\kappa = 0.41$ is the von Karman constant, d_w is wall distance. The blending function f_d is zero inside boundary layer

to deactivate the DES limiter and protect the boundary layer from earlier separation.

2.2. 6DoF rigid body solver

There has already been a standard 6DoF rigid body motion solver in OpenFOAM. In this 6DoF solver, the rigid body motion state is described by quaternions. While in the marine and ocean engineering context, an Euler angle description of motions for marine structures is preferred for convenience. Therefore, an in-house 6DoF solver based on Euler angles for marine hydrodynamic applications was adopted in naoe-FOAM-SJTU (Shen and Wan, 2013). Two coordinates frames, namely inertia and non-inertia frame, are used to describe the motions of the rigid body. The inertial frame or Earth frame is fixed to Earth or moves at a constant speed with respect to the Earth. The non-inertial frame or body-fixed frame is fixed on the rigid body and translates and rotates according to the motions of rigid body with respect to the inertial system. The two coordinate frames are related to each other by the position (x, y, z) (surge, sway, heave) and orientation, i.e., Euler angles (ϕ, θ, ψ) (roll, pitch, yaw) of the rigid body in Earth frame. The transformation of linear velocity (u, v, w) and angular velocity (p, q, r) from body-fixed frame to the earth-fixed frame can be done by two transform matrix J_1 and J_2 (Shen et al., 2015). The 6DoF rigid-body equations of motion are obtained by applying Newton's Second Law of Motion and governed by the following equations in body-fixed coordinate frame

$$\begin{cases} \dot{u} = X/m + vr - wq + x_g(q^2 + r^2) - y_g(pq - \dot{r}) - z_g(pr + \dot{q}) \\ \dot{v} = Y/m + wp - ur + y_g(r^2 + p^2) - z_g(qr - \dot{p}) - x_g(qp + \dot{r}) \\ \dot{w} = Z/m + uq - vp + z_g(p^2 + q^2) - x_g(rp - \dot{q}) - y_g(rq + \dot{p}) \\ \dot{p} = \frac{1}{I_x}\{K - (I_z - I_y)qr - m[y_g(\dot{w} - uq + vp) - z_g(\dot{v} - wp + ur)]\} \\ \dot{q} = \frac{1}{I_y}\{M - (I_x - I_z)rp - m[z_g(\dot{u} - vr + wq) - x_g(\dot{w} - uq + vp)]\} \\ \dot{r} = \frac{1}{I_z}\{N - (I_y - I_x)pq - m[x_g(\dot{v} - wp + ur) - y_g(\dot{u} - vr + wq)]\} \end{cases} \tag{8}$$

where m is the mass and I_x, I_y, I_z are the moments of inertia around the center of rotation, X, Y, Z, K, M and N are surge, sway, heave forces and roll, pitch, and yaw moments, respectively. (x_g, y_g, z_g) is the coordinate of center of gravity. By solving the 6DoF motion equations, the linear and angular accelerations in the body-fixed frame are obtained. The linear and angular velocities in the body-fixed frame are obtained by integrating acceleration over time and then they are transformed to earth-fixed frame. Finally, the translations and rotations increments are obtained by integrating velocities over time and they are used in the next stage for grid motion. The current implementation of 6DoF motion solver reserves an interface of generalized external forces such that mooring forces and constant force can be easily added on the body.

2.3. Mooring system

Mooring system consists of several mooring lines. Each mooring line is anchored to a fixed point at one end and attached to the moving body at the other end. The framework of mooring system follows the object-oriented (OO) design approach and OpenFOAM data structures. An abstract base class named *mooringLine* is designed for describing general mooring line. This class provides interfaces such as computing forces and moments (around center of rotation), updating mooring line shapes. These member functions will be implemented in derived classes for different types of mooring lines. Currently supported mooring line types include *linearSpring*, *catenary*, *PEM* (piecewise extrapolation method) and *LMM* (lumped mass method). It is easy to extend the mooring system and add new mooring line types based on the current framework thanks to the OO design. Finally, a wrapper *PtrList* < *mooringLine* > is used for the whole mooring system that consisting all kinds of mooring lines, as shown in Fig. 1. The solution procedure of mooring system is as summarized as follows: compute mooring forces and moments and add them as external excitation to the rigid body motion equations; solve the 6DoF motion equations and update motion state for the rigid body; update the mooring line shape for the current time step and go to next time step. In the present study, all mooring lines are treated as linear springs.

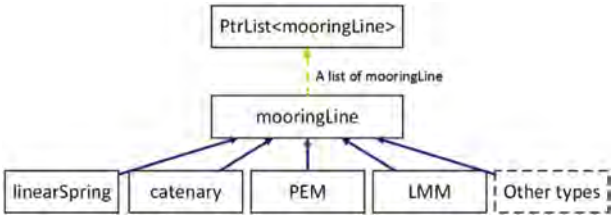

Fig. 1. Framework of mooring system module.

2.4. Overset grid

The naoe-FOAM-SJTU uses an overset grid system to solve the flow field. This is achieved by the combination of the grid assembly Suggar++ (Noack et al., 2009) and OpenFOAM. Details of the coupling strategy can be referred to Shen's work (Shen et al., 2015) and only a brief introduction is presented here.

A parallel scheme is archived in naoe-FOAM-SJTU by running OpenFOAM and Suggar++ processors simultaneously. Suggar++ is responsible for computing DCIs that contain cell type information (e.g., active, hole, orphan, fringe and donor) and interpolating weighting factors. OpenFOAM is responsible for solving fluid, computing forces and motions of the rigid body, and updating mesh. DCIs are sent from Suggar++ to OpenFOAM processors with MPI. Currently, Suggar++ does not support OpenFOAM mesh format, a copy of overset mesh will be converted from OpenFOAM format to Suggar++ supported format before computation. In other words, the solver keeps two separated grid instance, one for OpenFOAM and one for Suggar++. The Suggar++ grid is updated with the rigid body motion state obtained by OpenFOAM.

2.5. Solution strategy

The overall solution strategy is illustrated in Fig. 2. At the beginning

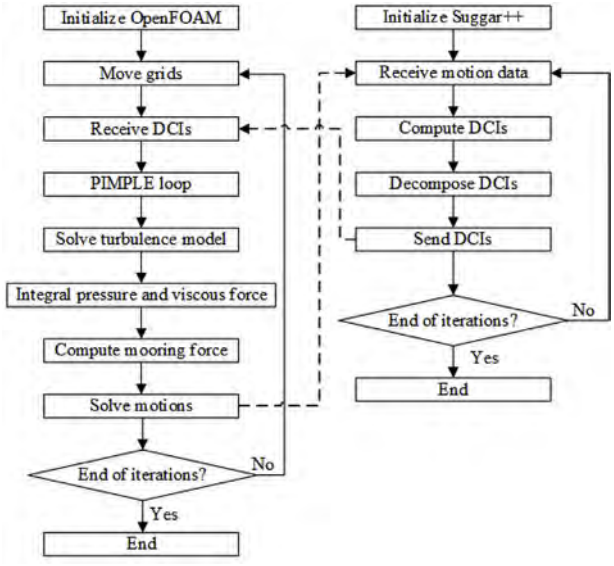

Fig. 2. Flow chart of the whole solution strategy.

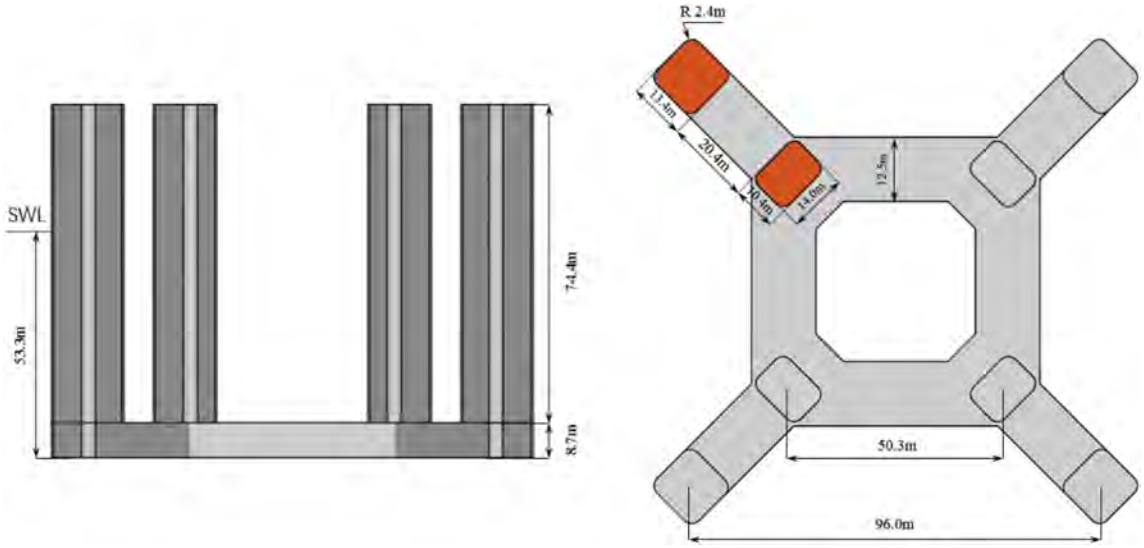

Fig. 3. Side view and top view of the prototype geometry.

of the simulation, OpenFOAM read meshes, boundary conditions and initial conditions for initialization. After that OpenFOAM receives DCIs from Suggar++, performs PIMPLE loop to obtain pressure and velocity and solves transport equations for turbulence quantities. Then pressure, viscous and mooring forces are computed and motions are predicted. The motion data will be sent to Suggar++ to update grids used by Suggar++. The DCIs in Suggar++ processor is decomposed by OpenFOAM's domain decomposition and cell distribution information and will be sent to each OpenFOAM processor.

3. Simulation design

3.1. Geometry and conditions

The geometry is a paired-column semi-submersible (PC Semi), which is a model used in the RPSEA 5404 project (Gordon and Mostofi, 2014). Fig. 3 shows the dimensions of prototype in side view and top view. The column height and pontoon height are 74.4 m and 8.2 m, respectively, resulting in an overall height of 82.6 m. The draft is 53.3 m. Columns are divided into outer column (OC) and inner column (IC). OCs are connected to ICs at four corners via pontoon at four corners of the pontoon. Both OC and IC have rectangular section, with difference sizes of 14 × 13.4 m and 14 × 10.4 m, respectively. The base gap between OC and IC is 20.4 m, and tensioner stroke is 8.5 m. The model scale (1:54) for PC Semi in the present numerical study is the same as that in model test. The main particulars of the PC Semi geometry in both full-scale and model-scale can be found in Table 1.

The case conditions consist of two parts: the stationary drag and the VIM simulation. In the stationary drag simulation, the semi-submersible is fixed and not allowed to move. Static overset grid is used for the stationary drag simulation. In this approach, as the hull is stationary and grids do not move, DCIs are computed at the beginning of the simulation and do not need to be updated in the following time steps. VIM simulation utilizes dynamic overset grid to perform hull boundary movement. In every time step, the DCIs are reinitialized automatically to update the hole-cutting geometry. Motions in horizontal plane (e.g., surge, sway and yaw) are allowed during VIM simulation.

3.2. Coordinate system and grids

A right-handed Cartesian coordinate system *O-XYZ* is used in the simulations. The origin *O* is located at the center point of hull geometry on the surface water line. *X*-axis coincides with current direction and points towards the downstream. *Y*-axis points to the transverse direction (starboard) that perpendicular to current and *Z*-axis points upwards.

Table 1
Main particulars of the prototype and model.

Name	Notation (unit)	Prototype	Model
Overall width	B (m)	113.4	2.1
Draft	T (m)	53.3	0.987
Immersed column height above pontoon	H (m)	44.6	0.826
Outer column size	$L_{OC} \times W_{OC}$ (m)	13.4 × 14	0.248 × 0.259
Outer column characteristic length	D (m)	19.4	0.36
Inner column size	$L_{IC} \times W_{IC}$ (m)	10.4 × 14	0.192 × 0.259
Inner column characteristic length	d (m)	17.4	0.32
Center-to-center distance of outer column	S_{OC} (m)	96.0	1.78
Center-to-center distance of inner column	S_{IC} (m)	50.3	0.93
Pontoon height	P (m)	8.2	0.16
Pontoon width	L_p (m)	12.5	0.23

The computational domain is set as $7B \times 4B \times 3.5T$ (length × width × depth) for all simulations as shown in Fig. 4. Here, B is the overall width and T is the draft of the hull. In previous studies of semi-submersible VIM, the computational domain sizes are slightly different. Kim et al. (2011) used a domain of $14B \times 12B \times 4.5T$. A $27B \times 18B \times 6T$ domain was adopted by Tan et al. (2013), and $18B \times 12B \times 6T$ by Liu et al. (2017a). Compared with these domains, smaller domain size is also acceptable. For example, Lee et al. (2014)

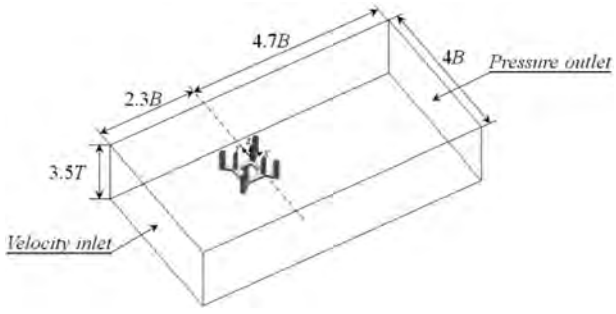

Fig. 4. Computational domain and boundaries.

numerically studied VIM of a deep-draft semi-submersible using computational domains of $6B \times 4.5B \times 2.8T$ and $5B \times 4B \times 2.2T$. A $9B \times 6B \times 3T$ domain was selected by Liang and Tao (2017) in their studies of vortex shedding process of flow around a deep-draft semi-submersible. It is then arguable that the current domain size is large enough to eliminate effect from boundaries at two lateral sides, downstream and bottom.

A constant and uniform flow condition is employed for all simulations. The boundary condition for the velocity is set as (U, 0,0) (U the current velocity) at inlet and zero gradient at outlet. As for pressure, a zero gradient boundary condition and zero value is set for the inlet and the outlet, respectively. Symmetry planes are specified for two lateral sides and bottom boundaries. Besides, symmetric boundary condition is also applied for the top boundary due to the neglect of free surface effect at low Froude number conditions. For hull surface of the PC Semi, a no-slip boundary condition is prescribed which assigns the velocity to $\mathbf{U}_{wall}$ and the pressure to zero normal gradient.

An unstructured polyhedral multi-block overset grid system is used throughout the present study. The grid system consists of two blocks, namely the background and hull grid, which are generated individually and then assembled into a single mesh. The background mesh block is hexahedral and has a uniform grid spacing S_b. The hull mesh block is based on predominantly Cartesian cut-cell approach and has a same initial base grid size with background mesh block to avoid orphans when performing overset DCI calculation. The near hull and wake regions are refined in the hull mesh block in order to capture the boundary layers and wake structures induced by flow separations. Four different levels of refinement zones are utilized to archive high accuracy in critical regions. In the vicinity of columns and pontoons, 10 prism cell layers are applied to hull boundary to capture the boundary layer development. For all cases, the non-dimensioned wall distance of the first layer satisfies $y+ < 1$ to make sure that the first layer cells are in the viscous sublayer. Fig. 5(a) illustrates the mesh size in refinement region and Fig. 5(b) shows the surface mesh on the hull.

DES resolves scales in the wake regions after flow separation. Thus, it is vital to avoid excessive numerical dissipation, which is guaranteed by discretizing all terms in governing equations using high-order schemes. The temporal derivatives in both momentum and turbulence quantities equations are discretized by second-order backward differencing scheme. A second-order upwind scheme, stabilized for transport (linear-upwind stabilized transport, LUST) is applied for convection term in momentum equation. For turbulent quantities convection terms, a second-order Total Variation Diminishing (TVD) limited linear scheme is used. The merged PISO-SIMPLE (PIMPLE) algorithm is used for pressure-velocity decoupling.

Table 2
Main particular for mass and stiffness system at model scale.

Name	Value	Dimensions
Mass	490.2	kg
Radius of gyration	0.77593	m
Transverse stiffness	173.98	N/m
Yaw stiffness	5.23	Nm/deg
Transverse natural period	15.45	s
Yaw natural period	9.32	s

3.3. Mooring stiffness

The most vital part of mooring system is not the configuration of the mooring lines but the equivalent restore stiffness provided by the mooring system. As the stiffness has direct influence on the moored floating body's natural period which significantly affect the VIM response characteristics. To make the comparison with experimental data meaningful, one must verify the effective stiffness before VIM simulation. In the experiments (Antony et al., 2015b), the model was equipped with frictionless air bearings that slide along a horizontal plate. This air bearing system allows the model to move freely in the horizontal plane. Meanwhile, the vertical motions are constrained. Table 2 lists the mass and stiffness properties of the hull and mooring system from experiment.

In the present numerical simulations, linear springs are used to construct an equivalent horizontal mooring system. Compared with catenary, PEM and LMM, linear springs are easier to adjust the horizontal global mooring stiffness. The mooring system consists of four linear springs that distribute along positive and negative X-axis and Y-axis. Fig. 6 depicts the sketch of the mooring system. All spring are pretensioned and the pretension should be large enough to ensure that the spring would not relax during VIM.

To perform validation for stiffness, static offset tests and free decay tests are carried out in sequence. In static offset tests, the hull is prescribed to move in Y-axis and rotate around Z-axis, respectively, without solving the flow field. Parameters such as stiffness and pretension of each spring are adjusted to match the global horizontal and vertical (yaw) stiffness in the model test. After static offset test, the spring parameters are used for free decay tests. The free-decay tests allow the hull to oscillate with a prescribed initial offset or velocity in the absence of inflow. Transverse and yaw decay test are conducted separately to verify the natural transverse and yaw period of the mooring system. The time histories and spectral analyses of free decay test are shown in Fig. 7. The deviations of natural period between CFD and EFD for transverse motion and yaw are 0.6% and 2%, respectively,

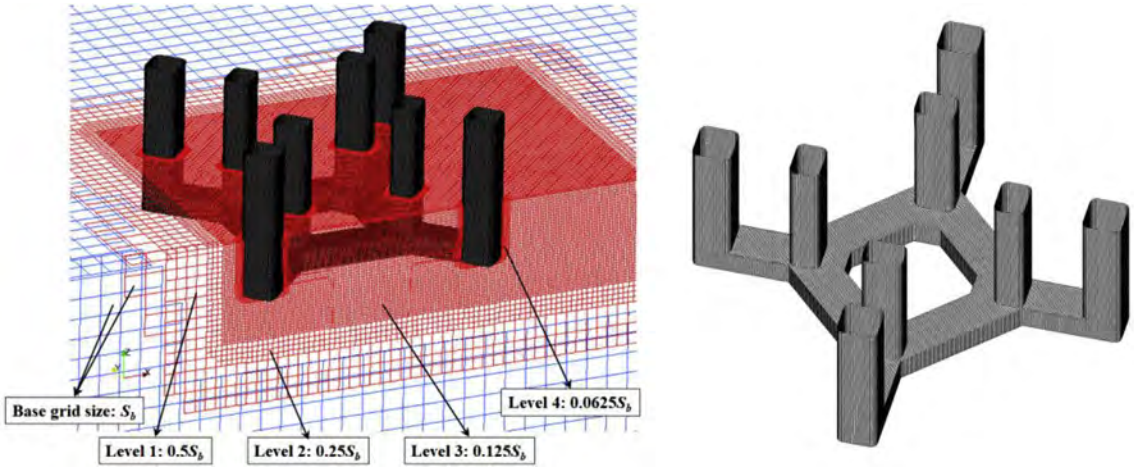

Fig. 5. Overset mesh assembly and hull surface mesh.

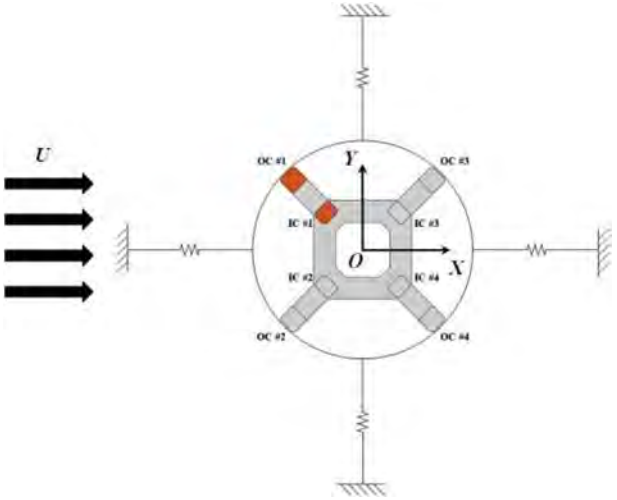

Fig. 6. Schematic of the mooring system configuration.

which indicates the correct equivalent linear and rotational stiffness are provided by the current mooring configuration.

4. Results and discussion

4.1. Stationary drag simulation

In this case, the current velocity is 0.272 m/s. The time step is set to 0.02s in all simulations, corresponding to a dimensionless time step of $\Delta tU/D$ is 0.015. This ensures the mean Courant number of the whole domain is smaller than 0.05 and the maximum Courant number is smaller than 5. Grid convergence study is performed on this case. Three different mesh sizes are considered. Note that the overset mesh blocks used in the current study is unstructured grid. The background mesh block is uniform hexahedral mesh and is easy to refine in three directions of the Cartisian coordinate system. Contrary to background, the hull mesh block is obtained by cut and splitting cells in refinement region on an initial Cartisian grid. Following the recommendation by

Table 3
Grid independent study for stationary drag simulation.

Case	ID	No. of cells ($\times 10^6$)			$\overline{C_D}$	C_{Lrms}
		Total	Background	Hull		
Fine	S_1	6.25	0.29	5.96	0.673	0.021
Medium	S_2	2.53	0.10	2.43	0.689	0.022
Coarse	S_3	1.04	0.04	1.00	0.726	0.048
EFD		–	–	–	0.683(± 3.0%)	–

Shen et al. (Shen and Wan, 2013; Shen et al., 2015), to achieve consistent grid refinement ratio in three directions, the Cartisian grid is refined systematically by a factor. Table 3 lists the details of different cases in grid sensitivity study. Grid refinement ratio $r = 1.4$ is selected for convergence study. Total grid number for coarse, medium and fine mesh are 1.04×10^6, 2.53×10^6 and 6.25×10^6, respectively. The grid independent study shows that S_2 can capture the wake behind columns and vortex sheds from lateral sides of columns. It can predict the drag and lift force accurately. Therefore, S_2 is fine enough to get reliable results at a relatively low computational cost and it is used in the following studies.

Fig. 8 shows the instantaneous flow visualizations presented by streamwise velocity contour and streamlines on two cut-planes at $z/H = -0.5$ and $z/H = -1$. It can be seen that wake interference between side-by-side OCs is insignificant. However, the wake behind front OC is strongly influenced by the front IC. Asymmetric wake is observed due to the speed up between front OC and IC. The wake interaction between front and rear ICs is clear due to the small spacing ratio ($L/d = 2.89$). As for front and rear OCs, the spacing ratio ($L/D = 4.95$) is large enough that the wake interference is trivial. Fig. 8(b) shows the existence of pontoon suppresses vortex sheds from the front OC inner flank. The coherent vortical structures along column vertical direction is destroyed at the low end by pontoon. This indicates the damp effect of pontoon on VIM behavior.

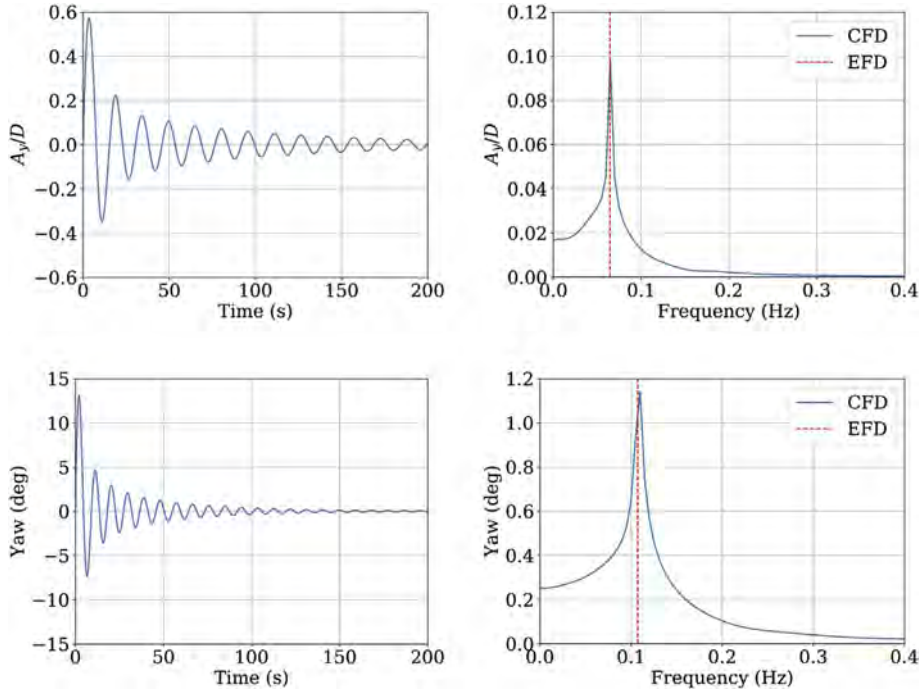

Fig. 7. Time history and spectral analysis of transverse and yaw decay test.

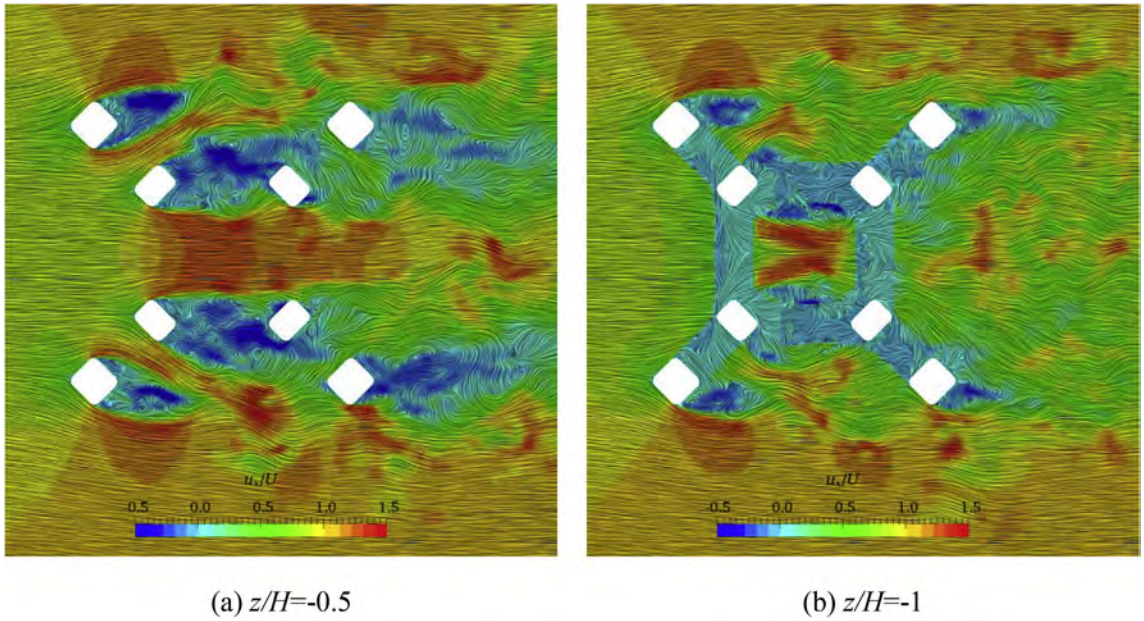

Fig. 8. Instantaneous streamwise velocity contours and streamlines.

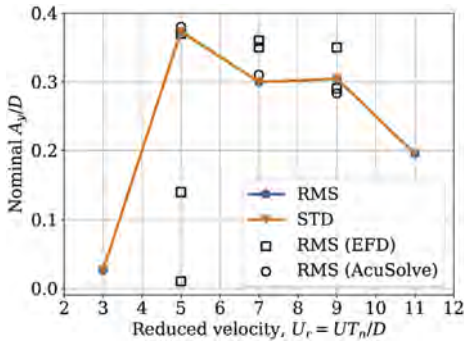

Fig. 9. Nominal response of transverse motion (EFD and AcuSolve data taken from (Antony et al., 2015b)).

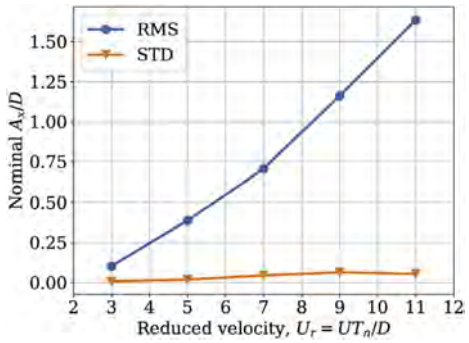

Fig. 10. Nominal response of in-line motion.

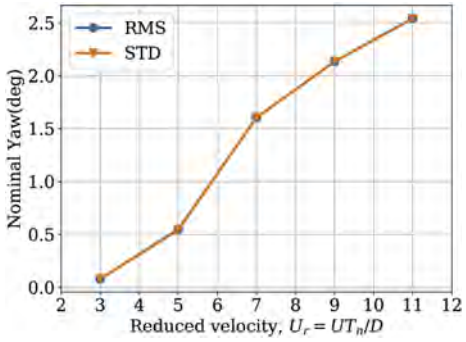

Fig. 11. Nominal response of yaw motion.

4.2. VIM simulation

The non-dimensioned parameter reduced velocity is crucial to VIM response. It is defined as

$$U_r = \frac{UT_n}{D} \tag{9}$$

where U is the current velocity or towing velocity, T_n is the natural transverse period in still water and D is the characteristic length of the platform. In previous studies of semi-submersible VIM, see for example (Waals et al., 2007; Rijken and Leverette, 2008; Gonçalves et al., 2011), D was the projected length of column section perpendicular to flow direction. While in the current study, $D = 0.36$ m, is the diagonal length of OC's cross section. This definition is consistent with model test.

Five reduced velocities are considered. The model-scale current speeds range from 0.07 m/s to 0.26 m/s. All the VIM simulations in this section keep the same time step with the stationary drag simulation. The corresponding Reynolds numbers are in the order of 10^4. When discussing motion characteristics of VIM, two sets of non-dimensional nominal responses are used throughout the present study. One is based on the root mean square (Zou et al., 2013; Antony et al., 2015a; Gritskevich et al., 2011) and the other is based on standard deviation (Waals et al., 2007) of motion response time series. The corresponding definitions are listed below

$$(A_x/D)_{rms} = \frac{\sqrt{2}RMS(A_x(t))}{D},\ (A_y/D)_{rms} = \frac{\sqrt{2}RMS(A_y(t))}{D},\ (Yaw)_{rms} = \sqrt{2}RMS(yaw(t)) \tag{10}$$

$$(A_x/D)_{std} = \frac{\sqrt{2}\sigma(A_x(t))}{D},\ (A_y/D)_{std} = \frac{\sqrt{2}\sigma(A_y(t))}{D},\ (Yaw)_{std} = \sqrt{2}\sigma(yaw(t)) \tag{11}$$

Where RMS and σ are the root mean square and standard deviation from motion time series, respectively, $A_x(t)$, $A_y(t)$ and $yaw(t)$ are time

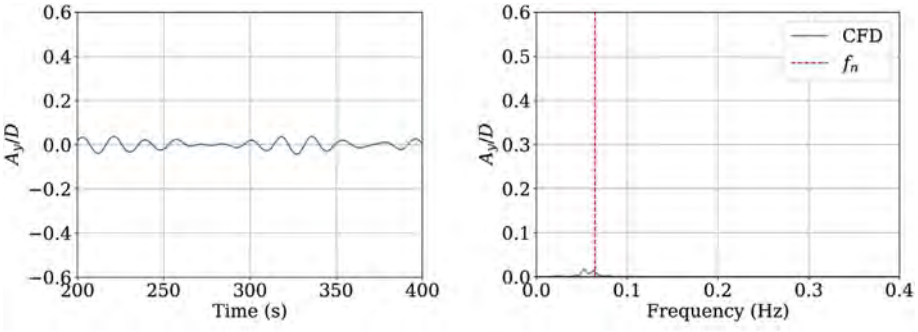

(a) U_r=3

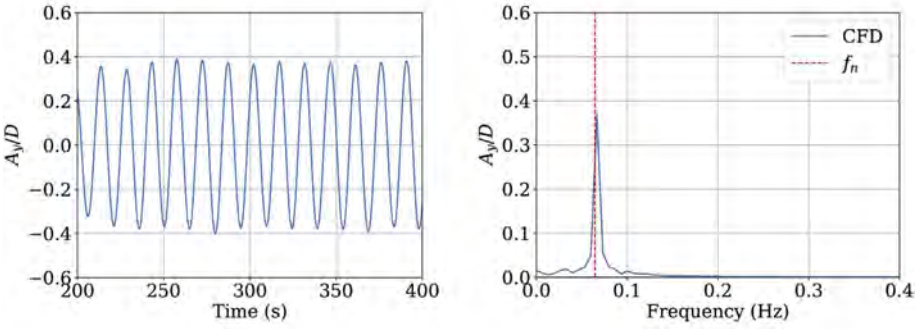

(b) U_r=5

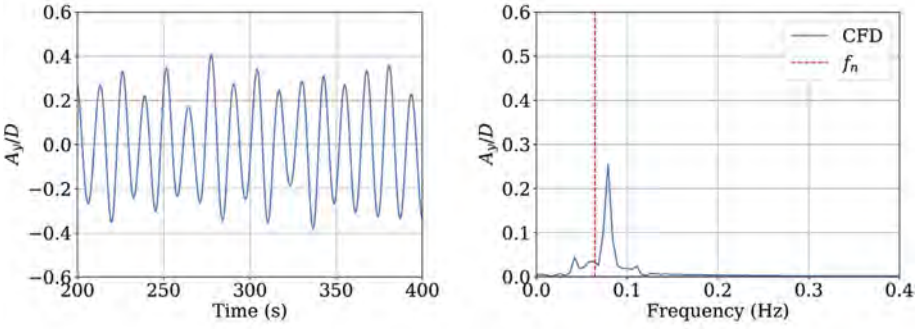

(c) U_r=7

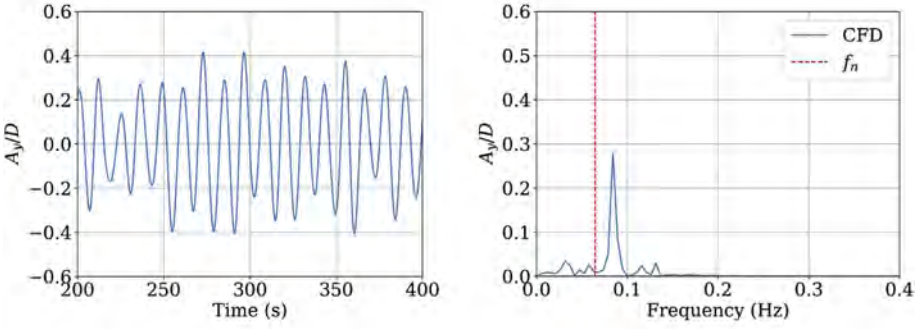

(d) U_r=9

Fig. 12. Time history and spectral analysis of transverse motion.

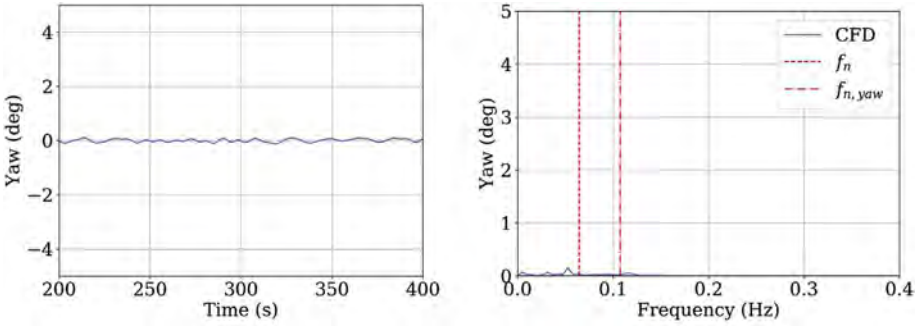

(a) U_r=3

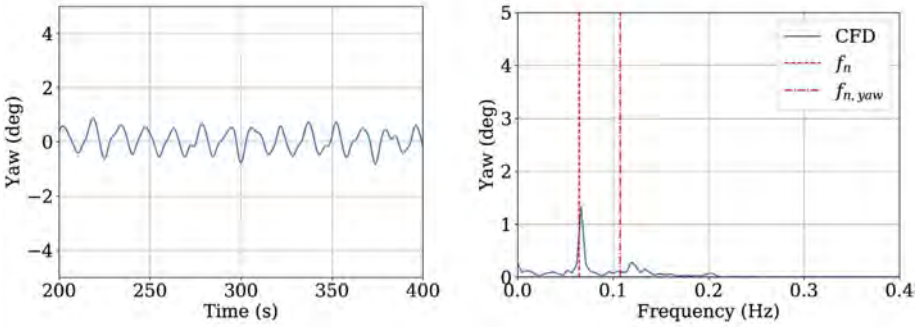

(b) U_r=5

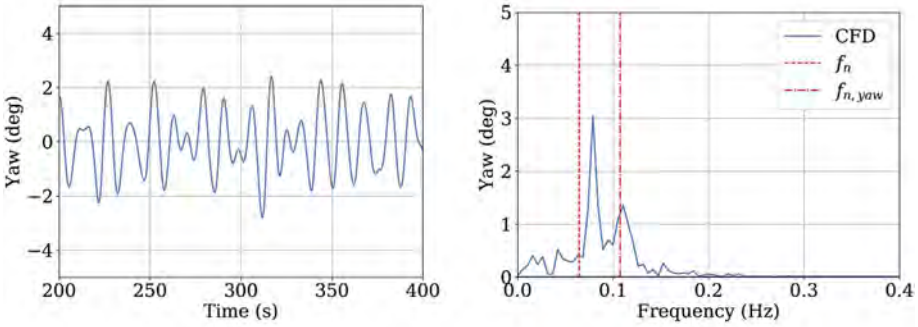

(c) U_r=7

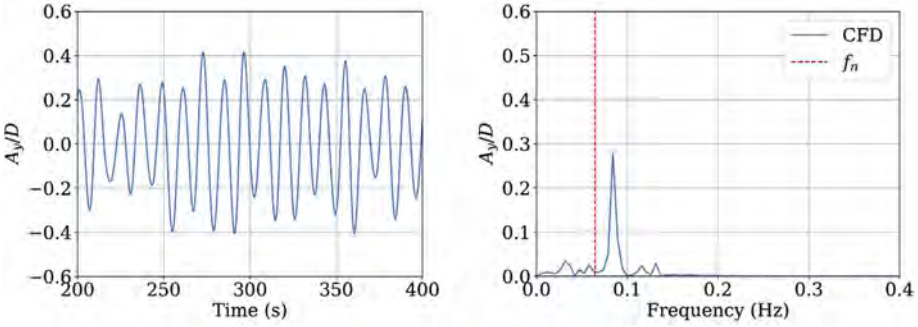

(d) U_r=9

Fig. 13. Time history and spectral analysis of yaw motion.

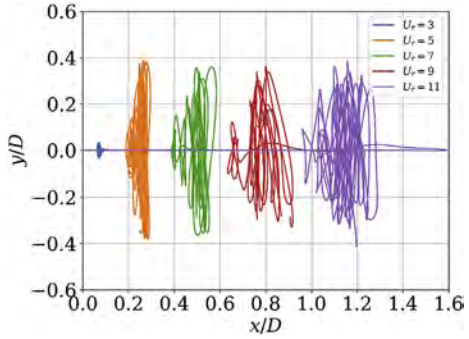

Fig. 14. Motion trajectories of centroid at different reduced velocities.

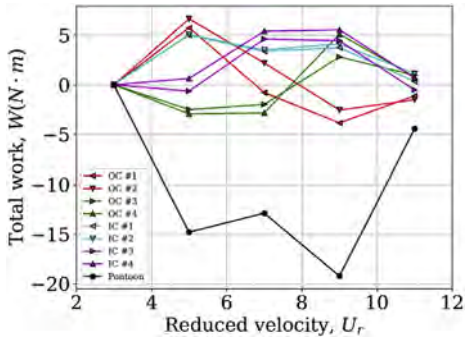

Fig. 15. Total work done by each component.

histories for in-line, transverse and yaw motions, respectively. To better representing the VIM characteristics, the transition stage at the beginning of VIM response is eliminated for all simulations when performing statistical analysis and spectral analysis.

The nominal response in transverse direction is plotted in Fig. 9. The black hollow square and circle represent the experimental data and CFD results taken from (Antony et al., 2015b). It's worth noting that the results at $U_r = 5$ from model test have large dispersion for three repeated runs. In CFD simulations, it takes longer time (40 dimensionless time step) for this particular case to reach pseudo steady state (quasi-sinusoidal transverse motion). This can be interpreted as the beginning of the lock-in range. The vibrational energy stored in the system is increasing slowly at this condition. This was also found by Chen and Chen (2016) in their CFD simulations of a deep draft semi-submersible. They stated that for a rounded-corner column semi-submersible at $U_r = 6$ for model scale and at $U_r = 4.4$ for prototype, a thousand more time steps is needed to reach the nominal amplitudes. As the current velocity increases, the vibrational energy increases more rapidly and the time to reach nominal amplitude decreases. The discrepancy between the results of the present CFD and AcuSolve simulations is rather small. Both CFD results deviate from EFD with variation no more than 15%. There could be a few possibilities for the discrepancy. Firstly, the mooring line settings may affect the experimental measurements, as the springs in the current numerical simulations are theoretically linear and the mooring line in model test are pretensioned vertical springs which could provide nonlinear stiffness at large motion amplitudes. Secondly, there could be some measurement error due to the towing facilities, because even in the lock-in range at $U_r = 9$, the nominal sway response differs from repeated towing condition by 16%. Thus, it is reasonable to say that the current approach of VIM simulation can be considered reliable.

The RMS and STD are of complete coincidence, which means the average position of transverse motion is near 0. When reduced velocity is small ($U_r = 3$), the nominal transverse motion response is rather small (about 0.02). As the reduced velocity increases, the nominal response increases promptly, suggesting a synchronized behavior in transverse motions ($5 \leq U_r \leq 9$). The maximum amplitude is up to 0.37 and it occurs at the beginning of lock-in range ($U_r = 5$).

Fig. 10 shows the nominal response in the in-line direction. RMS represents the average offset to origin and STD represents the fluctuation of VIM in in-line direction. For immersed structure exposed to current, the overall drag on structure increases with the current velocity increases. The offset between equilibrium position and origin becomes larger. This explains the increasing RMS of in-line response. Compared with transverse motion, the STD of in-line motion is small, which indicates much smaller fluctuation of in-line response. In addition, larger STD values are found at higher reduced velocities ($9 \leq U_r \leq 11$), which may be caused by the unsteady natural of the force and moment in post-lock-in range.

Similarly, Fig. 11 shows the nominal response of yaw motion. The nominal yaw motion is monotonically increasing and reaches to about 2.55° at $U_r = 11$. As is mentioned previously, the natural yaw period ($T_{n,yaw} = 9.32$s) is much smaller than the natural transverse period ($T_n = 15.45$s). Obviously, yaw motion has a much higher natural frequency. Amongst the current cases, even the highest reduced velocity does not reach the range which synchronization occurs between vortex shedding and yaw motions. Redefining reduced velocity by yaw natural period $U_{r,yaw} = \frac{UT_{n,yaw}}{D}$, $U_r = 11$ is corresponding to $U_{r,yaw} = 6.6$, which is exactly the lock-in range in terms of yaw. We have no reason to doubt that as current velocity continually increasing, the nominal yaw response may still increase but eventually decrease when it comes to the post-lock-in range in terms of yaw.

To better understanding the motion characteristics at different reduced velocities, further spectral analyses are performed for transverse, in-line and yaw motions. Fig. 12 depicts the time history and FFT spectral analysis results for transverse motion at different reduced velocities. At low reduced velocity ($U_r = 3$), the small and irregular motion response with multiple frequencies suggest a motion state before lock-in. After entering lock-in range, the transverse motion is characterized by a dominant frequency which can be clearly seen in Fig. 12(b)-(d). This confirms the strong modulated transverse motion in lock-in range. Unlike VIV, in which the shedding frequency is locked on one natural frequency in a wide range of reduced velocities (see for example (Khalak and Williamson, 1999)), the motion frequency of semi-submersible does not lock on one particular frequency. Instead, it increases as the increasing of reduced velocity. This may be attributed to the complex hull geometry (e.g., the multi-column structure and pontoon).

Similar to transverse motion, the time history and FFT spectral analysis for yaw motion are detailed in Fig. 13. At pre-lock-in regime (e.g., $U_r = 3$), yaw is fluctuating at small amplitude like transverse motion. When entering lock-in range ($U_r = 5$), dominant frequency occurs and characterizes the yaw motion. It should be emphasized that as the reduced velocity continually increases, a second dominant frequency appears near yaw natural frequency. The first peak frequency is undoubtedly the consequence of vortex shedding, as it is coincidence with the transverse motion frequency at corresponding velocity. This corroborates that the yaw motion of semi-submersible is induced by vortex shedding. The phenomenon was termed vortex-induced yaw or VIY (Gonçalves et al., 2012). The occurrence of the second dominant frequency is induced by the interaction, particularly the synchronization between yaw motion and vortex shedding. This was previously reported by Gonçalves et al. (2012) in their model test of a large-volume semi-submersible platform. The existence of VIY shows the importance of yaw motions together with transverse motions in the VIM study of semi-submersibles. It also increases the difficulty and complexity to estimate the fatigue failure of risers and mooring system for semi-submersibles.

Fig. 14 plots the motion trajectories of the hull centroid on horizontal plane. No typical “eight (8) shape” trajectory is observed for all conditions. In the lock-in range, the synchronized behavior results in

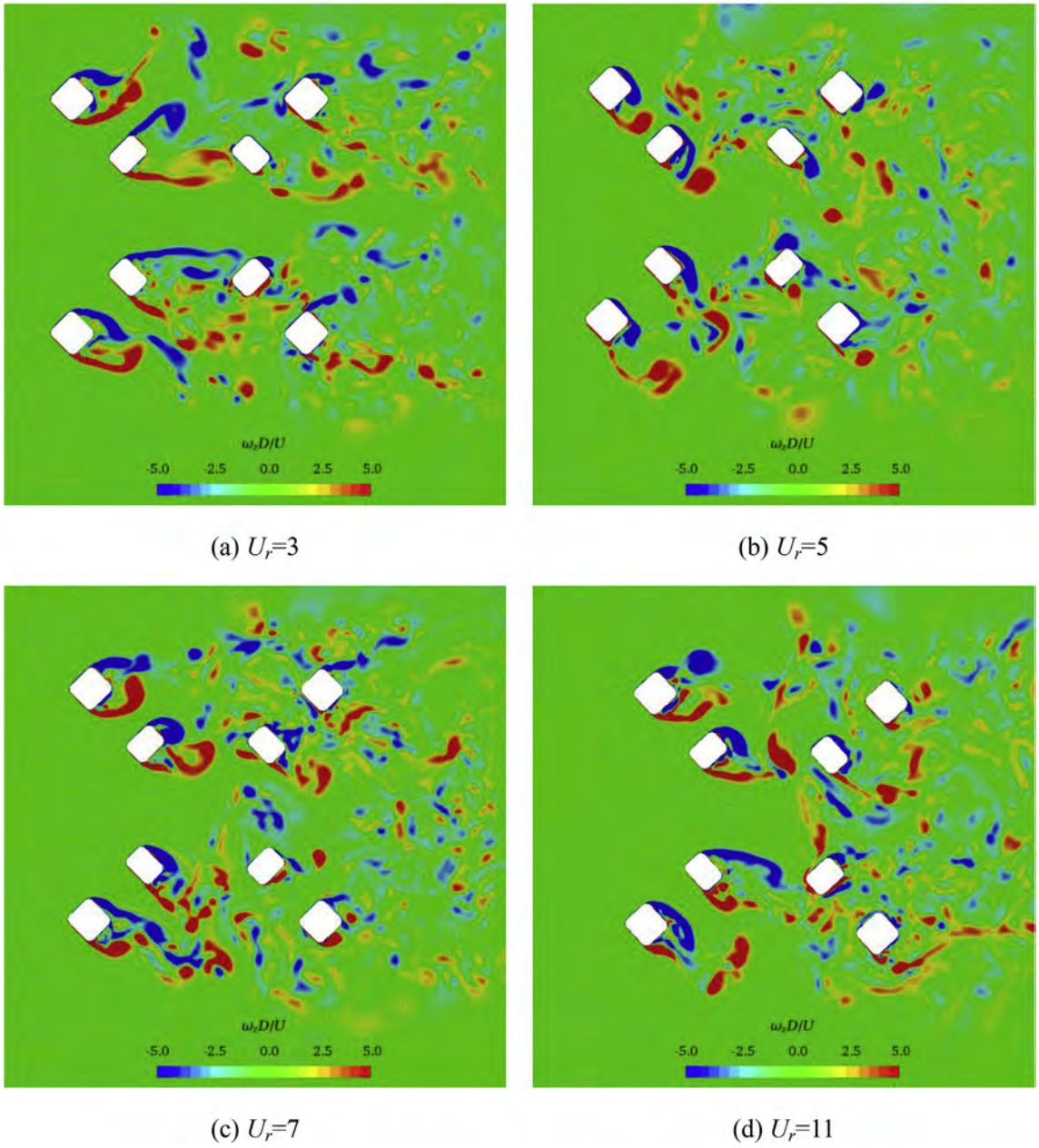

Fig. 16. Instantaneous non-dimensional spanwise vorticity contour at half draft ($z/H = -0.5$) plane.

pronounced transverse motion amplitude. The transverse motion response in post-lock-in range is the same magnitude to that in lock-in range. However, the in-line response fluctuates much stronger in pre-lock-in range. Trajectories at higher reduced velocities become more erratic.

To analysis the effect of columns and pontoon on VIM characteristic, the work done by each component during stabilized VIM are calculated and presented in Fig. 15. The work done is calculated with the following formula (Liu et al., 2017b)

$$W_x = \int F_x(t)\cdot\dot{x}(t)dt$$
$$W_y = \int F_y(t)\cdot\dot{y}(t)dt$$
$$W = W_x + W_y \tag{12}$$

where W_x and W_y is work done in the in-line and transverse directions, respectively. W is total work done. $F_x(t)$ and $F_y(t)$ are hydrodynamic force on each component in the in-line and transverse directions, respectively.

For convenience, the columns are labeled by numbers. The definition can be found in Fig. 6. The overall work done by pontoon is negative for all reduced velocities. The magnitude of negative work done by pontoon are much larger than a single column, suggesting that pontoon could effectively mitigate VIM response. At low reduced velocity (U_r = 5), the excitations of VIM are mainly from upstream columns (OC #1 and #2, IC #1 and #2). The downstream OCs damp VIM a little and ICs have nearly no effects on VIM. However, this is not always the case. The work done by two upstream OCs turn from positive to negative at high reduced velocity (U_r = 9). On the contrary, the work done by other columns except two upstream OCs are all positive. The reason for this change is unclear yet. A possible explanation may be attributed to the complex wake interaction in this unique design of paired-column hull structure, as the work done transition from positive to negative did not observed in previous study of conventional four-column semi-submersibles (Zhao and Wan, 2016; Liu et al., 2017b).

Fig. 16 presents the instantaneous spanwise vorticity contour at different reduced velocities. The vorticity is non-dimensionalized by the

characteristic length and current velocity. The vortex shedding mainly occurs at two lateral rounded corners for each upstream column. Vortices shed from upstream column directly impinge on the downstream column, then collide and interact with the vortices shed from downstream columns. These vortices quickly break into small eddies in the wake region of downstream columns. As U_r increases to 5, VIM enteris lock-in scenario, the vortex shedding patterns changes distinctively. Synchronized vortex shedding patterns are clearly observed amongst the four upstream columns. Moreover, the vortices generated from two lateral rounded corner are reattaching to the backface of each upstream column after flow separation. This dramatically increases the hydrodynamic force and motion amplitude in transverse direction.

5. Conclusions

Stationary drag and VIM simulations of a paired-column semi-submersible at model scale are performed using an in-house CFD solver naoe-FOAM-SJTU. The turbulence flow is modeled with SST-DES method and the motions are obtained by solving 6DoF equations. Dynamic overset grid is used to prevent the near wall mesh distortion during large yaw motions. Results from stationary drag simulations show that the current DES turbulence is applicable to accurately predict the drag of complex multi-column hull geometry. Several reduced velocities range from 3 to 11 are investigated for VIM. The transverse motion responses predict by the current numerical approach are in good agreement with CFD results by Antony et al. (2015b). Spectral analysis using FFT for transverse and yaw motion time series are conducted. The transverse motion in lock-in scenario is governed by dominant frequency equivalent to vortex shedding frequency. Unlike VIV, the vortex shedding frequency in VIM of semi-submersible does not lock on one natural transverse frequency. It increases as the current velocity increases. FFT results for yaw response show that yaw motion is induced by vortex shedding. Synchronized behavior for yaw motion occurs when shedding frequency is approaching yaw natural frequency. The work done by pontoon is always negative, suggesting the damping effect of pontoon on VIM response. The flow reattachment on the backface of upstream columns, together with the synchronized vortex shedding between multiple upstream columns, account to for the pronounced VIM motion in lock-in range.

Acknowledgement

This work is supported by the National Natural Science Foundation of China (51490675, 11432009, 51579145), Chang Jiang Scholars Program (T2014099), Shanghai Excellent Academic Leaders Program (17XD1402300), Program for Professor of Special Appointment (Eastern Scholar) at Shanghai Institutions of Higher Learning (2013022), Innovative Special Project of Numerical Tank of Ministry of Industry and Information Technology of China (2016-23/09) and Lloyd's Register Foundation for doctoral student, to which the authors are most grateful.

References

Antony, A., Vinayan, V., Halkyard, J., Kim, S.-J., Holmes, S., Spernjak, D., 2015a. A CFD based analysis of the Vortex Induced Motion of deep-draft semisubmersibles. In: Proceedings of the 25th International Ocean and Polar Engineering Conference. Kona, Big Island, Hawaii, USA, ISOPE, vol. 3. pp. 1048–1055.

Antony, A., Vinayan, V., Holmes, S., Spernjak, D., Kim, S.J., Halkyard, J., 2015b. VIM study for deep draft column stabilized floaters. In: Proceedings of the Offshore Technology Conference. Houston, Texas, USA, OTC-25837-MS.

Cao, H., Wan, D.C., 2010. Application of OpenFOAM to simulate three-dimensional flows past a single and two tandem circular cylinders. In: Proceedings of the 20th International Offshore and Polar Engineering Conference. Beijing, China, ISOPE, vol. 3. pp. 702–709.

Chen, C.-R., Chen, H.-C., 2016. Simulation of vortex-induced motions of a deep draft semi-submersible in current. Ocean Eng. 118, 107–116.

Finnigan, T., Roddier, D., 2007. Spar VIM model tests at supercritical Reynolds numbers. In: Proceedings of OMAE 2007. San Diego, California, USA, OMAE2007–29160.

Gonçalves, R.T., Nishimoto, K., Rosetti, G.F., Fujarra, A.L.C., Oliveira, A.C., 2011. Experimental study on vortex-induced motions (VIM) of a large-volume semi-submersible platform. In: Proceedings of OMAE 2011. Rotterdam, The Netherlands, OMAE2011–49010.

Gonçalves, R.T., Rosetti, G.F., Fujarra, A.L.C., Luís, A., Nishimoto, K., Oliveira, C., 2012. Vortex-Induced Yaw motion (VIY) of a large-volume semi-submersible platform. In: Proceedings of the 22nd International Offshore and Polar Engineering Conference. Rhodes, Greece, ISOPE, vol. 3. pp. 572–578.

Gordon, R., Mostofi, R., 2014. Ultra-deepwater Dry Tree System for Drilling and Production in the Gulf of Mexico. RPSEA Report (10121-4405-02). .

Gritskevich, M.S., Garbaruk, A.V., Schütze, J., Menter, F.R., 2011. Development of DDES and IDDES formulations for the k-ω shear stress transport model. Flow Turbul. Combust. 88 (3), 431–449.

Kara, M., Kaufmann, J., Gordon, R., Sharma, P., Lu, J., 2016. Application of CFD for computing VIM of floating structures. In: Proceedings of the Offshore Technology Conference. Houston, Texas, USA, OTC-26950-MS.

Khalak, A., Williamson, C.H.K., 1999. Motions, forces and mode transitions in vortex-induced vibrations at low mass-damping. J. Fluid Struct. 13, 813–851.

Kim, J.-W., Magee, A., Guan, K.Y.H., 2011. CFD simulation of flow-induced motions of a multi-column floating platform. In: Proceedings of OMAE 2011. Rotterdam, The Netherlands, OMAE2011–49437.

Kim, S.J., Spernjak, D., Holmes, S., Vinayan, V., Antony, A., 2015. Vortex-Induced Motion of floating structures: CFD sensitivity considerations of turbulence model and mesh refinement. In: Proceedings of OMAE 2015. St. John's, Newfoundland, Canada, OMAE2015–42221.

Lee, S.-K., Chien, H.-P., Gu, H., 2014. CFD study of deep draft semisubmersible VIM. In: Proceedings of the Offshore Technology Conference Asia. Kuala Lumpur, Malaysia, OTC-24766-MS.

Liang, Y., Tao, L., 2017. Interaction of vortex shedding processes on flow over a deep-draft semi-submersible. Ocean Eng. 141, 427–449.

Liu, M., Xiao, L., Yang, J., Tian, X., 2017a. Parametric study on the vortex-induced motions of semi-submersibles: effect of rounded ratios of the column and pontoon. Phys. Fluids 29 055101.

Liu, M., Xiao, L., Liang, Y., Tao, L., 2017b. Experimental and numerical studies of the pontoon effect on vortex-induced motions of deep-draft semi-submersibles. J. Fluid Struct. 72, 59–79.

Menter, F.R., Kuntz, M., Langtr, R., 2003. Ten years of industrial experience with the SST turbulence model. Turbul. Heat. Mass Transf 4, 625–632.

Noack, R.W., 2005. SUGGAR: a general capability for moving body overset grid assembly. In: Proceedings of the 17th AIAA Computational Fluid Dynamics Conference. Toronto, Ontario, Canada, AIAA 2005–5117.

Noack, R.W., Boger, D.A., Kunz, R.F., Carrica, P.M., 2009. Suggar++: an improved general overset grid assembly capability. In: Proceedings of the 19th AIAA Computational Fluid Dynamics Conference. San Antonio, Texas, USA, AIAA 2009–3992.

Rijken, O., Leverette, S., 2008. Experimental study into vortex induced motion response of semi submersibles with square columns. In: Proceedings of OMAE 2008. Estoril, Portugal, OMAE2008–57396.

Roddier, D., Finnigan, T., Liapis, S., 2009. Influence of the Reynolds number on spar Vortex Induced Motions (VIM): multiple scale model test comparisons. In: Proceedings of OMAE 2009. Honolulu, Hawaii, USA, OMAE2009–79991.

Rosetti, G.F., Gonçalves, R., Fujarra, A.L.C., Koop, A., 2016. CFD calculations of the vortex-induced motions of a circular-column semi-submersible. In: Proceedings of OMAE 2016. Busan, Korea, OMAE2016–54987.

Shen, Z., Wan, D., 2013. RANS computations of added resistance and motions of a ship in head waves. Int. J. Offshore Polar Eng. 23, 263–271.

Shen, Z., Wan, D., Carrica, P.M., 2015. Dynamic overset grids in OpenFOAM with application to KCS self-propulsion and maneuvering. Ocean Eng. 108, 287–306.

Tan, J.H.C., Magee, A., Kim, J.W., Teng, Y.J., Zukni, N.A., 2013. CFD simulation for vortex induced motions of a multi-column floating platform. In: Proceedings of OMAE 2013. Nantes, France, OMAE2013–11117.

van Dijk, R.R.T., Fourchy, P., Voogt, A., Mirza, S., 2003. The effect of mooring system and sheared currents on vortex induced motions of truss Spars. In: Proceedings of OMAE 2003. Cancun, Mexico, OMAE2003–37151.

Vinayan, V., Antony, A., Halkyard, J., Kim, S.-J., Holmes, S., Spernjak, D., 2015. Vortex-induced motion of deep-draft semisubmersibles: a CFD-based parametric study. In: Proceedings of OMAE 2015. St. John's, Newfoundland, Canada, OMAE2015–42209.

Waals, O.J., Phadke, A.C., Bultema, S., 2007. Flow induced motions of multi column floaters. In: Proceedings of OMAE 2007. San Diego, California, USA, OMAE2007–29539.

Wang, J., Zou, L., Wan, D.C., 2017. CFD simulations of free running ship under course keeping control. Ocean Eng. 141, 450–464.

Zhao, W., Wan, D.C., 2016. Detached-eddy simulation of flow past tandem cylinders. Appl. Math. Mech. 37 (12), 1272–1281.

Zhao, W., Shen, Z., Wan, D., 2014. Numerical investigation of the vortex induced motion of SPAR in uniform current. In: Proceedings of the 24th International Ocean and Polar Engineering Conference. Busan, Korea, ISOPE, vol. 3. pp. 362–367.

Zhou, H., Cao, H., Wan, D.C., 2013. Numerical predictions of wave impacts on the supporting structures of Shanghai Donghai-Bridge offshore wind turbines. In: Proceedings of the 23rd International Offshore and Polar Engineering Conference. Anchorage, Alaska, USA, ISOPE, vol. 1. pp. 216–224.

Zou, J., Poll, P., Roddier, D., Tom, N., Peiffer, A., 2013. VIM testing of a paired column semi submersible. In: Proceedings of OMAE 2013. Nantes, France, OMAE2013–10001.